

Polarization Lidar at Summit, Greenland, for the Detection of Cloud Phase and Particle Orientation

RYAN R. NEELY III,* MATTHEW HAYMAN,⁺ ROBERT STILLWELL,[#] JEFFREY P. THAYER,[#] R. MICHAEL HARDESTY,[@] MICHAEL O'NEILL,[&] MATTHEW D. SHUPE,** AND CATHERINE ALVAREZ⁺⁺

* *Department of Atmospheric and Oceanic Science, University of Colorado, and CIRES, and NOAA/Earth System Research Laboratory/GMD, and NOAA/Earth System Research Laboratory/CSD, Boulder, Colorado*

⁺ *Advanced Studies Program, National Center for Atmospheric Research, Boulder, Colorado*

[#] *Department of Aerospace Engineering Sciences, University of Colorado, Boulder, Colorado*

[@] *NOAA/Earth System Research Laboratory/CSD/Atmospheric Remote Sensing, Boulder, Colorado*

[&] *Earth Science and Observation Center, CIRES, and NOAA/Earth System Research Laboratory/GMD, Boulder, Colorado*

^{**} *CIRES, and ATOC, University of Colorado, and NOAA/Earth System Research Laboratory/PSD, Boulder, Colorado*

⁺⁺ *NOAA/Earth System Research Laboratory, GMD, Boulder, Colorado*

(Manuscript received 4 May 2012, in final form 5 November 2012)

ABSTRACT

Accurate measurements of cloud properties are necessary to document the full range of cloud conditions and characteristics. The Cloud, Aerosol Polarization and Backscatter Lidar (CAPABL) has been developed to address this need by measuring depolarization, particle orientation, and the backscatter of clouds and aerosols. The lidar is located at Summit, Greenland (72.6°N, 38.5°W; 3200 m MSL), as part of the Integrated Characterization of Energy, Clouds, Atmospheric State, and Precipitation at Summit Project and NOAA's Earth System Research Laboratory's Global Monitoring Division's lidar network. Here, the instrument is described with particular emphasis placed upon the implementation of new polarization methods developed to measure particle orientation and improve the overall accuracy of lidar depolarization measurements. Initial results from the lidar are also shown to demonstrate the ability of the lidar to observe cloud properties.

1. Introduction

Clouds and aerosols modulate the surface energy and ice mass budgets in polar regions (Francis and Hunter 2006; Kay et al. 2008; van den Broeke et al. 2009). Any alteration in the current climatology of clouds and aerosols will have large impacts on their role in both of these budgets. Remote sensing of the vertical distribution, backscatter, and linear volume depolarization of particles in the atmosphere has been shown to greatly contribute to this knowledge by constraining their radiative parameters (Sassen et al. 2003; Hansen et al. 2011).

As with all remote sensing techniques, the determination of thermodynamic phase of hydrometeors by

linear polarization lidar is subject to many uncertainties from measurements and assumptions in the retrieval of physical parameters from raw data (Russell et al. 1979; Sassen 2005; Hu et al. 2009; Nott et al. 2012; Hayman and Thayer 2009). A significant assumption in conventional lidar depolarization ratio methods is that the observed particles are randomly oriented (Kaul et al. 2004; Hu et al. 2009). This assumption has been shown to bias cloud phase estimates, when viewed from near zenith, toward higher assignment of liquid water and inhibit accurate measurement and analysis of cloud phase by depolarization lidar (Hu et al. 2009; Takano 1989; Chepfer and Brogniez 1998; Hayman and Thayer 2012). It has also been well documented, through observations of optical phenomena such as sun dogs and halos, that this assumption is clearly not valid for a proportion of observations (Lynch et al. 1994; Hu et al. 2009; Noel and Chepfer 2010).

It should be noted that only certain habits of ice crystals will orient horizontally because orientation is a

Corresponding author address: Ryan Reynolds Neely III, Department of Atmospheric and Oceanic Science, UCB 311, University of Colorado, Boulder, CO 80309-0311.
E-mail: ryan.neely@colorado.edu

bulk property of a population of ice crystals with similar aerodynamic properties. The habits of ice crystals are quite variable and are strongly dependent on the supersaturation of ice and temperature where the crystal is formed and grows (Magono and Lee 1966; Bailey 2009). Kaul et al. (2004) found that the orientation of particles with large azimuthal diameters is more likely to be horizontally oriented, but observations of these particles are obscured by a larger population of smaller, randomly oriented particles. This leads current observations to determine mean particle parameters that undercharacterize the amount of particle orientation in clouds. The horizontally oriented ice crystals (HOIC) discussed here are ideally thought of as hexagonal plates but the observations shown here, in reality, result from populations of ice crystals that are platelike (i.e., flatter) around their preferred orientation.

With conventional depolarization lidars, cloud phase is often classified by interpreting the ratio of two perpendicular polarization channels in conjunction with the relative amount of observed backscatter. This ratio, conventionally assigned to the symbol δ , is often called the depolarization ratio. The ability to identify cloud phase using the depolarization ratio was recognized by Schotland et al. (1971) and is based on the assumption that near-spherical liquid water droplets will produce low linear depolarization ratios, while nonspherical ice crystals will produce high linear depolarization ratios. Implicit to this interpretation is that the scattering volume is optically thin, such that multiple scattering of spherical particles is not the cause for higher depolarization ratios (e.g., Pal and Carswell 1973), and that the particles within this volume are randomly oriented, such that backscatter from oriented ice crystals is not the cause for low depolarization ratios. These issues have been generally treated by correlating the depolarization ratio with the relative amount of observed backscatter. Postprocessing algorithms developed for the Cloud-Aerosol Lidar with Orthogonal Polarization (CALIOP) *Cloud-Aerosol Lidar and Infrared Pathfinder Satellite Observations (CALIPSO)* mission have been implemented and demonstrated to help distinguish multiple scattering and oriented ice crystals effects in characterizing cloud phase (Hu et al. 2009; Noel and Chepfer 2010).

The dataset from near-nadir (0.3°) CALIOP observations indicated a clear population of oriented ice crystals when organized into the scattering regime of high backscattered signals with low depolarization ratios. This proved to be a useful approach in identifying oriented ice crystals. In comparison, the off-nadir (3°) CALIOP dataset no longer observed this characteristic scattering regime. However, the off-nadir measurement

does not preclude the presence of oriented ice crystals from the dataset but moves them into another regime of the backscatter-to-depolarization-scattering relationship that is not clearly separable from randomly oriented ice crystals. It is known that when horizontal ice crystals are viewed obliquely, the backscatter strength decreases substantially while the depolarization ratio increases (Platt et al. 1978). Thus, when viewed obliquely the scattering characteristics of horizontally oriented ice crystals are similar in backscatter strength and depolarization ratio to randomly oriented ice crystals (Sassen 2005; Noel and Chepfer 2010). In fact, many lidar systems operate at oblique angles to avoid the strong specular backscatter signal by horizontally oriented ice crystals and the adverse effects these signals have on detector performance. Therefore, polarization lidar systems measuring only depolarization ratios and operating obliquely are not capable of resolving HOIC from randomly oriented ice crystals through depolarization and backscatter measurements. Those lidar systems operating normal to HOIC can use indirect methods of correlating backscatter strength to depolarization ratios but, because of the large dynamic range of the specular and nonspecular signals, the performance of the system is often compromised. A scanning lidar system can monitor the change in depolarization ratio with incident angle to help identify HOIC, but it still relies on interpretation and assumptions of the scattering volume. This was notably done first by Thomas et al. (1990) and has been followed by many studies, including Noel and Sassen (2005).

Recently, Hayman and Thayer (2012) addressed this issue by exploring the general polarization properties of atmospheric scatterers and particularly of HOIC. They showed through forward polar decomposition of scattering matrices that HOIC can display the polarization properties of depolarization, retardance, and diattenuation. They note that the commonly estimated depolarization ratio does not make any distinction between scattering matrix types but only indicates whether the polarization properties have changed. It is not until the form of the scattering matrix is truly of a randomly oriented particle description that the depolarization ratio has a physical polarization definition. The scattering matrix for oriented particles cannot be attributed to any single polarization effect. Hayman and Thayer (2012) indicate that diattenuation, which is a polarization-dependent scattering efficiency, is displayed by oriented particles when viewed at oblique scattering angles. This is a property that cannot be exhibited by randomly oriented particles, and thus it can be used to identify HOIC in oblique lidar backscatter observations. The goal of this paper is to describe a multiple linear polarization

lidar system designed to observe polarization signals indicative of HOIC and to demonstrate the benefits of such a configured lidar system for cloud and aerosol studies.

The Cloud, Aerosol Polarization and Backscatter Lidar (CAPABL) is located at Summit, Greenland (72.6°N, 38.5°W; 3200 m MSL) as part of the Integrated Characterization of Energy, Clouds, Atmospheric State, and Precipitation at Summit (ICECAPS) Project (Shupe et al. 2013). Despite the importance of clouds to Greenland's climate, recent studies indicate that little is known about the true cloud cover characteristics over Greenland (Griggs and Bamber 2008). Currently, the only observations of cloud microphysics made at Summit were reported in 1993 (Borys et al. 1993). The large uncertainty in cloud fraction and the lack of information on cloud microphysical properties inhibit our understanding of cloud radiative effects on the surface (Starkweather 2004). As a result, current models poorly represent clouds over the Arctic and more specifically over the Greenland Ice Sheet (GIS), and simulations of surface energy budgets and precipitation continue to be highly uncertain.

The goal of ICECAPS is to make measurements of the cloud, atmosphere, precipitation, and radiation properties over the GIS to address these issues (Shupe et al. 2013). Alongside the polarization lidar discussed here, an instrument suite consisting of a cloud radar, two microwave radiometers, an Atmospheric Emitted Radiance Interferometer, an X-band precipitation sensor, a ceilometer, a micropulse lidar, a sodar, and a twice-daily radiosonde program contribute to the ICECAPS dataset. Data from CAPABL will be used in conjunction with the other instruments at the observatory to help improve the understanding of Arctic clouds and climate processes by quantifying cloud occurrence, vertical distribution, microphysical composition, and radiative properties. This information can then be used to better constrain the next generation of forecast and climate models. Current data and analysis software may be found online (at <http://www.esrl.noaa.gov/psd/arctic/observatories/summit/browser/>).

While CAPABL's primary objective, as part of ICECAPS, is to identify tropospheric cloud phase, the ability of the lidar to identify HOIC removes ambiguity in the interpretation of linear depolarization ratios. The lidar is also part of the National Oceanic and Atmospheric Administration (NOAA)'s Earth System Research Laboratory's Global Monitoring Division's (GMD) lidar network. In this role, the lidar uses traditional backscatter retrieval methods to measure aerosol profiles into the lower stratosphere (Russell et al. 1979; Barnes and Hofmann 1997; Hofmann et al. 2009). CAPABL

was deployed to Summit in June of 2010 and has run continuously (24-h operation) since that time except for short periods of maintenance and further instrument development. CAPABL is the newest addition to the Arctic network of lidars and because of its location on top of the GIS it is one of the few lidars that will be minimally impacted by regional change (Nott and Duck 2011).

Atmospheric diattenuation measurements are a relatively new concept. The implementation of this ability in CAPABL took several iterations and changes to the system before a positive identification of HOIC could be made. From June 2010 to April 2011, CAPABL was run in a near-zenith pointing direction. Observations from this period consist only of traditional polarization lidar measurements. In May 2011 CAPABL was tilted about 11° off zenith. As described in the polarization method section, this instrument setup allowed CAPABL to detect nonzero diattenuation values that would be indicative of backscattered signals from HOIC. Efforts to validate diattenuation signals from these observations led to the need to rule out the impacts of detector saturation. This was resolved in November 2011 by adding a fourth polarization channel with opposite sensitivity to detector saturation. This is described fully in the section detailing the polarization operation and sources of error. Since this time CAPABL has run continuously with the ability to discern actual diattenuation from systemic effects. In this manuscript, the focus is on describing the method and the implementation of the polarization scheme within the lidar system, a discussion of the errors associated with the scheme, and a demonstration of the lidar's ability to observe diattenuation signals.

2. Location

Summit Station (3200 m MSL) is the only dedicated atmospheric observatory operating continuously at high altitudes in the Arctic. Because of its elevation, Summit allows for almost direct access to the free troposphere and is relatively free of local influences that could corrupt free-tropospheric climatic records. The high altitude also allows CAPABL to easily observe the lower stratosphere. Summit is situated ideally for studies attempting to identify and understand long-range, intercontinental transport, such as the long-range transport of boreal forest fire smoke. While other Arctic atmospheric research observatories, such as those at Barrow, Alert, Ny Alesund, Tiksi, and Cherski, lie at sea level near coastal and continental influences, Summit is free of regional effects from increased shipping, melting ice, and thawing permafrost. Thus, changes in the

observational record from Summit should generally represent widespread Arctic trends or events that are sufficiently significant to have large-scale effects. This makes Summit an ideal location for observing processes that may be applicable to the larger GIS and the Arctic region.

Shupe et al. (2013) have shown that clouds occur approximately 80% of the time at Summit. As such, Summit is an ideal place to observe a wide range of Arctic clouds but optically thick clouds significantly inhibit lidar observations. Figure 1 provides an estimate of the relative occurrence of visible optical depths (ODs) observed at Summit. This plot is provided to estimate the amount of atmospheric conditions CAPABL will be able to observe. The plot suggests that for approximately 50% (where $OD < 2$) of the time, CAPABL will be able to profile the full troposphere. Figure 1 also indicates that for approximately 25% of the time, the OD is large enough (>4) that observations from CAPABL will be significantly attenuated.

3. Polarization theory

A polarization lidar system is completely described using the Stokes vector lidar equation (SVLE), which relates the Stokes vector of the transmitted light to the received photon counts in each observed

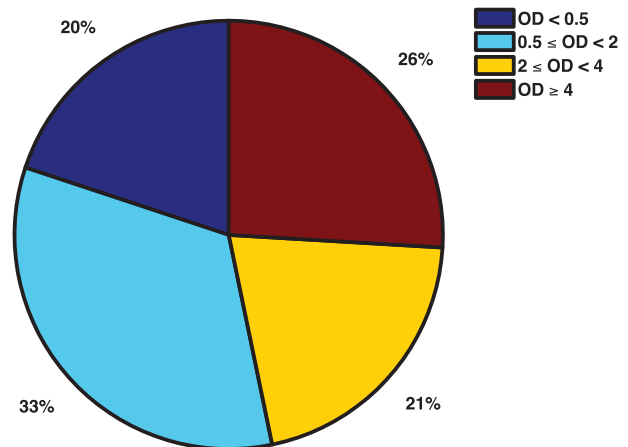


FIG. 1. Estimate ($\pm 10\%$) of the relative occurrence of visible ODs observed at Summit from June 2011 to April 2012. Estimates were retrieved from observations made by the Polar Atmospheric Emitted Radiance Interferometer (P-AERI) (Shupe et al. 2013).

polarization channel (Hayman and Thayer 2012). Besides the sought-after polarization properties of the scatterers in the atmosphere, all of the optical components within the lidar must be included to account for the possibility of polarization modification and cross talk by the optical system. Thus, the SVLE takes the form of

$$\mathbf{N} = \mathbf{O}\mathbf{M}_{\text{RX}} \left\{ \left[G(z) \frac{A}{z^2} \Delta z \right] \mathbf{T}_{\text{atm}}(\mathbf{k}_s, z) \mathbf{F}(\mathbf{k}_i, \mathbf{k}_s, z) \mathbf{T}_{\text{atm}}(\mathbf{k}_i, z) \mathbf{M}_{\text{TX}} \mathbf{S}_{\text{TX}} + \mathbf{S}_B \right\}, \quad (1)$$

where \mathbf{N} is a vector of the photon counts from the observed planes of polarization, \mathbf{O} is the output matrix describing the measurement channels, \mathbf{M}_{RX} is the receiver's Mueller matrix, \mathbf{T}_{atm} is the Mueller matrix accounting for atmospheric transmission, $\mathbf{F}(\mathbf{k}_i, \mathbf{k}_s, z)$ is the scattering phase matrix for the incident wavenumbers \mathbf{k}_i and \mathbf{k}_s at range z , and \mathbf{M}_{TX} is the Mueller matrix of the transmitter. For randomly oriented particles observed by a monostatic lidar, such as CAPABL, the scattering phase matrix assumes the form of (van de Hulst 1981; Flynn et al. 2007; Gimmestad 2008)

$$\mathbf{F}_r(\pi) = \begin{bmatrix} f_{11} & 0 & 0 & 0 \\ 0 & f_{22} & 0 & 0 \\ 0 & 0 & -f_{22} & 0 \\ 0 & 0 & 0 & f_{11} - 2f_{22} \end{bmatrix}. \quad (2)$$

Linear depolarization due to randomly oriented scatterers may be characterized from this scattering phase matrix by observing the parallel and perpendicular

polarization components of the backscattered light (Gimmestad 2008). The resulting photon count vector of Eq. (1) takes the form

$$\mathbf{N} = \begin{bmatrix} N_{\perp} \\ N_{\parallel} \end{bmatrix}. \quad (3)$$

The volume linear depolarization ratio δ takes the form

$$\delta = \frac{f_{11} - f_{22}}{f_{11} + f_{22}} = \frac{N_{\perp}}{N_{\parallel}}. \quad (4)$$

For randomly oriented scatterers, this measurement fully characterizes the depolarizing effect of the scattering volume. When HOIC are present in the scattering volume, off-diagonal elements of Eq. (2) become non-zero. Furthermore, δ no longer retains the traditionally assumed physical meaning derived from Eq. (2), as additional polarization effects contribute to the diagonal

elements as well (Hayman and Thayer 2012). When a scattering volume contains some mixture of oriented and randomly oriented nonspherical particles, the volume backscattered light will not only be depolarized but may also contain diattenuation and retardance. Thus, for proper interpretation of depolarization data, the orientation state of the scatterers must be known.

To collect the additional information needed to evaluate the assumption of randomly oriented scatterers, additional terms from the scattering matrix must be observed. The scattering phase matrix for a volume containing HOIC is given in Eq. (5) (Kaul et al. 2004; Hayman and Thayer 2012). One notable difference between the randomly oriented scattering phase matrix [Eq. (2)] and the oriented scattering phase matrix in Eq. (5) is the additional off-diagonal elements of \mathcal{F}_{12} and \mathcal{F}_{34} . These elements represent diattenuation properties of the scatterer (polarization-dependent scattering efficiency) and retardance, respectively, and a nonzero measurement of either of these terms would signify the presence of HOIC. It is also important to note the different notation between elements in Eqs. (2) and (5) with the diagonal elements in Eq. (2) not necessarily equal to the diagonal elements in Eq. (5):

$$\mathbf{F}_o(\mathbf{k}_i, -\mathbf{k}_i) = \begin{bmatrix} \mathcal{F}_{11} & \mathcal{F}_{12} & 0 & 0 \\ \mathcal{F}_{12} & \mathcal{F}_{22} & 0 & 0 \\ 0 & 0 & \mathcal{F}_{33} & \mathcal{F}_{34} \\ 0 & 0 & -\mathcal{F}_{34} & \mathcal{F}_{44} \end{bmatrix}. \quad (5)$$

The \mathcal{F}_{12} element represents linear diattenuation. Observing this term requires a third polarization measurement in addition to the perpendicular and parallel polarization measurements needed to estimate the volume linear depolarization ratio. In CAPABL’s setup (described below), this measurement is made at 45° compared to the parallel polarization channel. Therefore, CAPABL’s full vector of observed backscattered light is represented by

$$\mathbf{N} = \begin{bmatrix} N_{\perp} \\ N_{45} \\ N_{\parallel} \end{bmatrix}. \quad (6)$$

A depiction of CAPABL’s transmitted light and received polarizations in reference to a HOIC is found in Fig. 2. This measurement arrangement has been entitled the parallel-45-perpendicular (P45P) technique (Hayman 2011). From this measurement an assessment of the linear diattenuation term D_q may be defined in terms of the observable values of the lidar,

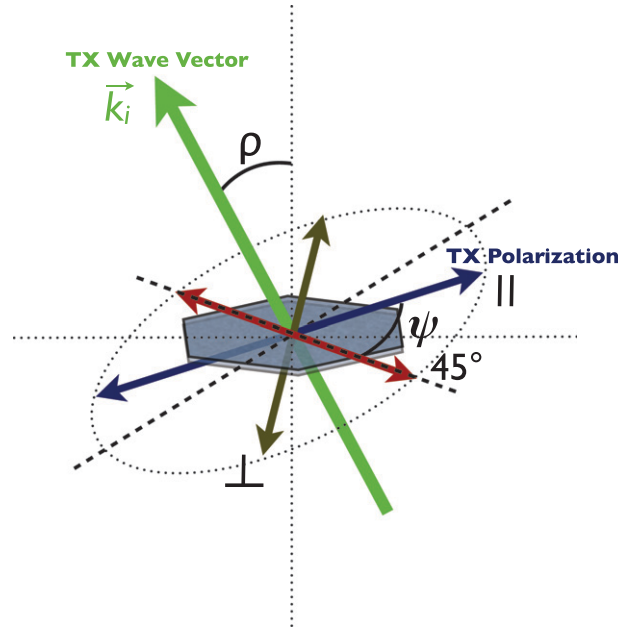


FIG. 2. Illustration of the polarization terms in reference to the lidar beam and horizontal scatterers. Lidar tilt angle (ρ , 11° for CAPABL) is measured relative to zenith (vertical axis), and the polarization angle ψ is measured relative to the linear polarization that lies in the horizontal plane (plane perpendicular to the \mathbf{k} of the transmitted light). Dashed oval represents the plane perpendicular to the vector of the transmitted beam.

$$D_q = \frac{\mathcal{F}_{12}}{\mathcal{F}_{11}} = \frac{2N_{45}}{N_{\parallel} + N_{\perp}} - 1. \quad (7)$$

Equation (7) represents the normalized linear diattenuation of the scattering matrix. If \mathcal{F}_{12} is zero, then the scattering matrix will take the form of Eq. (2). In the case of HOIC, \mathcal{F}_{12} is nonzero and linear diattenuation exists. For CAPABL’s particular geometry, δ takes the form

$$\delta = \frac{\mathcal{F}_{11} + \mathcal{F}_{33}}{\mathcal{F}_{11} - \mathcal{F}_{33}} = \frac{N_{\perp}}{N_{\parallel}}, \quad (8)$$

where $\mathcal{F}_{33} < 0$ due to the π phase shift from backscattering.

This value is observed using the traditional polarization ratio method, as in Eq. (4), but it should be interpreted with consideration that \mathcal{F}_{33} may depend on depolarization, diattenuation, and retardance (Hayman and Thayer 2012). Although symmetry conditions of oriented scatterers also allow for a nonzero \mathcal{F}_{34} , results reported by Kaul et al. (2004) suggest this term is generally small compared to linear diattenuation.

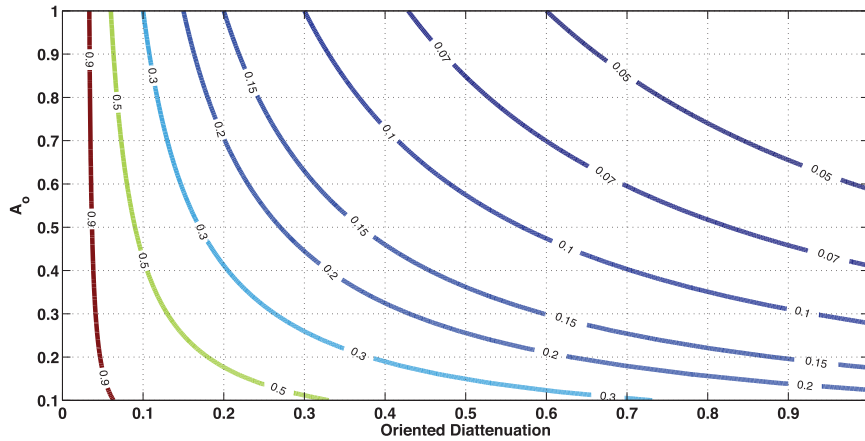


FIG. 3. Contour showing the minimum fraction of ice crystals that must be oriented if CAPABL's minimum resolvable diattenuation is 0.03. Results are plotted as a function of the oriented ice crystal diattenuation and the relative backscatter cross section of oriented to randomly oriented ice crystals.

The P45P method allows the lidar to forego the assumption that scatterers in the observation volume are randomly oriented. The presence of linear diattenuation unambiguously shows when this assumption is invalid and polarization data are affected. In the presence of HOIC, the data may still be observed and described in terms of δ , but they may not uniquely depend on one term from the scattering matrix and may not be equally compared to the δ of randomly oriented scatterers.

CAPABL's ability to detect the diattenuation of HOIC depends on its significance in the volume scattering matrix. The total volume matrix is a sum of all possible scatterers within the illuminated volume. Observations of the atmosphere will contain both oriented and randomly oriented scatterers, so the total observed scatter matrix may be defined as

$$\mathbf{F}_t = \mathbf{F}_o + \mathbf{F}_r, \quad (9)$$

where \mathbf{F}_o and \mathbf{F}_r are the backscatter matrices of all oriented scatterers described by Eq. (5) and randomly oriented scatterers represented by Eq. (2), respectively. Since we treat diattenuation as a normalized quantity, the total diattenuation of the volume is given by

$$\frac{f_{12}^t}{f_{11}^t} = \frac{\mathcal{F}_{12}}{\mathcal{F}_{11}} \frac{\mathcal{F}_{11}}{f_{11}^t}, \quad (10)$$

where the superscript t indicates the matrix element is from the total volume and the other matrix elements correspond to Eqs. (2) and (5). This means that as the fraction of backscatter signal from oriented ice crystals

decreases, the diattenuation of the volume will be diluted. The fraction of backscatter of oriented ice crystals will depend on the population fraction of oriented ice crystals, size distributions, tilt angles, and aspect ratios.

The oriented ice crystal exhibits a scattering cross section that is some fraction of the mean randomly oriented ice crystal cross section, so that

$$\sigma_o = A_o \sigma_r, \quad (11)$$

where σ_o is the oriented ice crystal backscattering cross section that is a function of the lidar tilt angle and σ_r is the mean randomly oriented backscattering cross section. The total measured backscatter must be equal to the sum of these cross sections weighted by their respective number densities,

$$f_{11}^t = \mathcal{F}_{11} + f_{11} = n_o \sigma_o + n_r \sigma_r. \quad (12)$$

The total scattering population must be the sum of the two subpopulations here ($n_T = n_o + n_r$), so substituting Eq. (11) and rearranging Eq. (12) provides the relative fraction of oriented ice crystals,

$$\frac{n_o}{n_T} = \frac{\frac{\mathcal{F}_{11}}{f_{11}^t}}{A_o - \frac{\mathcal{F}_{11}}{f_{11}^t} (A_o - 1)}. \quad (13)$$

We can then solve for the relative backscatter contribution of oriented ice crystals in Eq. (10) and substitute into Eq. (13) to obtain

$$\frac{n_o}{n_T} = \frac{\mathcal{F}_{12}}{A_o f_{12}^i - \mathcal{F}_{12}(A_o - 1)}. \quad (14)$$

We assume a minimum resolvable diattenuation of 0.03 (i.e., $f_{12}^i/f_{11}^i = 0.03$) and plot the minimum required population of oriented ice crystals as a function of A_o and the oriented ice crystal diattenuation f_{12}^o using Eq. (14). The resulting contour is shown in Fig. 3. The figure shows that to resolve an oriented ice crystal population that exhibits diattenuation of 0.5 and represents 10% of the scattering volume, the backscatter cross section of the oriented ice crystals must be approximately half of the mean backscatter cross section of the randomly oriented population.

Thus, the ability of the instrument to discern diattenuation is dependent on the angle of the ice crystal axis of symmetry and the \mathbf{k} of the lidar [see Eq. (5); Fig. 2]. For CAPABL, 11° was chosen to obtain the highest feasible ρ based on the existing system and observatory design. Studies of a 17-month *CALIPSO* dataset have suggested oriented ice crystal populations are typically less than 10% (Zhou et al. 2012; Noel and Chepfer 2010). However, *CALIPSO* has a much larger footprint at tropospheric altitudes than CAPABL, and it is not clear whether HOIC populations tend to be localized (which would result in higher population fractions for CAPABL) or evenly distributed over the entire cloud.

4. System description

CAPABL is based on NOAA's Earth System Research Laboratory's Chemical Science Division's (CSD) Depolarization and Backscatter Unattended Lidar (DABUL; Alvarez et al. 1998; Intrieri et al. 2002; Turner 2005). The structure of DABUL was unchanged, but the transmitter and the receiver were reconfigured to enable measurement of diattenuation for detecting HOIC. Modifications most notably include the use of a Meadowlark liquid crystal variable retarder (LCVR) and a new data acquisition system.

The CAPABL transmitter consists of a frequency-doubled, diode-pumped, neodymium-doped, yttrium lithium fluoride (Nd:YLF) laser operating at 523.5 nm (Fig. 4). The transmitted signal is first passed through a half-wave plate (HWP) and polarizing beam splitter (linear output polarization) to ensure maximum linear polarized power output. After the polarizer, the beam passes through an 80-times expander to achieve a divergence of 0.165 mrad. A back reflection of the beam, from a beam sampler, is incident on a trigger photodiode, which is the trigger to initiate the data acquisition. Two folding mirrors aligned in a periscope configuration

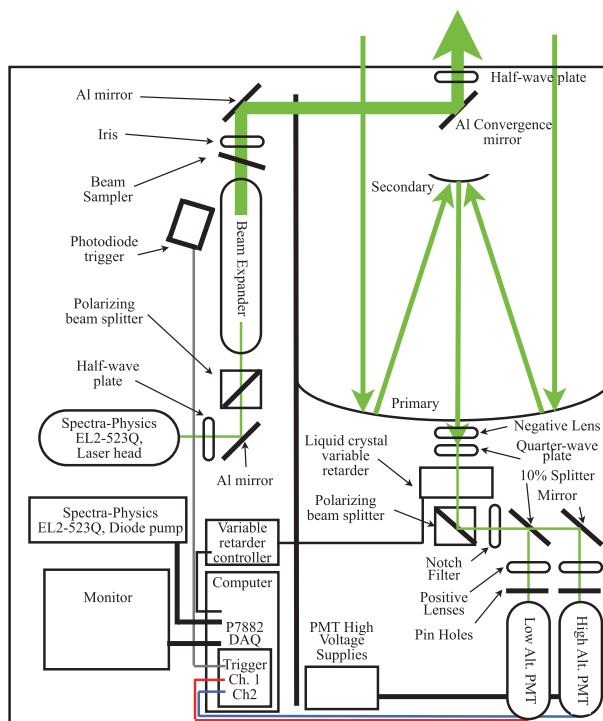


FIG. 4. Schematic layout of optics and main components of CAPABL. Lidar transmits a single linear polarization and detects linear polarizations parallel, perpendicular, and at 45° to the transmitted polarization.

direct the transmitted beam above the receiver secondary. This allows for a full overlap with the receiver field of view at 200 m, which is required for tropospheric studies. The several folding mirrors in the transmitter generally disrupt the linearly polarized input state. However, there always exists a linear input polarization that produces a linear output polarization. The HWP located directly in front of the laser is used to rotate transmitted beams' polarization in such a way that the combined impact of the following optical elements produces a purely linear polarization signal above the last mirror (located above the receiver's secondary mirror) (Hayman 2011). This results in a transmitted beam with a 99.6% degree of linearly polarized light. A final HWP above the convergence mirror allows for the rotation of this linearly polarized signal and defines the polarization axes of the lidar (all further references to transmitted or received polarization are in reference to this axis, which is at zero degrees when the polarization is in the S plane or horizontally polarized). To achieve the polarization measurements of diattenuation, described in the next section, the lidar output polarization is rotated (using the outgoing HWP) 45° to the reference horizontal polarization plane (see Fig. 3).

TABLE 1. CAPABL system specifications.

Transmitter	Receiver	Signal processing
(Spectra-Physics EL2–523Q diode-pumped Nd:YLF)	(Dall–Kirkham Cassegrain telescope configuration)	(Photon-counting data acquisition)
Wavelength: 523.5 nm (frequency doubled)	Receiver aperture: 35.6 cm	Data system:
Pulse energy: 25 μ J	Filter bandwidth: 0.3 nm	Fast Comtec P7882
Pulse rate: 2000 Hz	Channels: 2 (high, low)	Range bin size: 100 ns (30 m)
Divergence: 0.165 mrad	Field of view: 0.3 mrad, 0.7 mrad	One-line integration: 5 s
		PMTs: 2 (EMI 9863B/100)
		Linear dynamic range: \sim 2–3 MHz

The receiver consists of a F/14.3 Dall–Kirkham telescope with a 508-cm focal length and 35.6-cm aperture (see Table 1). This telescope design uses symmetric low angles of incidence on the mirrors, which minimizes polarization effects caused by the system. The collected light is then collimated by a 100-mm negative lens and passed through a horizontal quarter-wave plate (QWP), the LCVR oriented at 45°, and a polarizing beam splitter (horizontal polarizer). The combination of these polarization elements creates a rotating analyzer with a polarization angle controlled by the phase of the LCVR. After the polarizer, 10% of the signal is passed to the low-altitude photomultiplier tube (PMT) with low gain to avoid saturation from high-intensity signals below 1 km in altitude. The remaining 90% of the signal is passed to the high-gain channel for upper-tropospheric and lower-stratospheric data collection.

The combination of optical elements (Table 1) in the receiver creates an angle cone of approximately \sim 2° (full angle) for the low-altitude channel and \sim 1° (full angle) for the high-altitude channels. Mirrors are known to have both diattenuating and retarding polarization effects that can contribute error to polarization measurements. In addition, large angular spreads incident on mirrors can contribute a depolarization system effect due to variability in the mirror phase shift and diattenuation with angle. However, there are no beam-steering components prior to the polarization analyzer. As a result, the beam-steering elements in the receiver only ever see one polarization, and the polarization effects of

the steering mirrors have a negligible impact on polarization measurements.

The entire system is controlled by LabVIEW and is fully autonomous (including data transfer and processing) and runs continuously. Control of the lidar may also be done remotely. An operator is only required for hardware maintenance and modifications. The current observation specifications (including maximum range and resolution) of CAPABL for the observations of clouds in the troposphere and aerosol backscatter from the stratosphere may be found in Tables 2 and 3, respectively. Observations of the different polarization channels are made sequentially with a 5-s integration on each. Between each integration, 0.5 s is needed to download the data from the data acquisition system. This results in a total of 22 s to measure four polarization planes. This observation scheme was based on an analysis of the signal-to-noise requirements, measurement duty cycle, and anticipated temporal variability of the clouds. CAPABL has the ability to make measurements at a much faster rate but because of the hard limit of 0.5 s between each integration and slow temporal variation of Arctic stratiform clouds, a longer duty cycle was made default for observations in order to increase the signal-to-noise requirements of each observation and to reduce the dead time between them (Shupe et al. 2011).

5. Polarization operation and sources of error

CAPABL uses a LCVR sandwiched between a QWP and horizontal polarizer to create a polarization

TABLE 2. Polarization observation ranges and limits.

Property	Specification
Maximum range	5 km (above summit)
Vertical resolution	30 m
Temporal resolution	5.5 s per polarization
Observed polarizations	4
Uncertainty in linear depolarization ratio	2.5%

TABLE 3. Stratospheric aerosol observation ranges and limits.

Property	Specification
Maximum range	25 km MSL
Vertical resolution	300 m
Temporal resolution	4 h
Observed linear polarizations	4
Uncertainty in due to shot noise	8%

analyzer that can perform the three polarization measurements necessary for the observation method (Fig. 4). The LCVR has no capability to rotate in its mount, so its orientation defines the 45° polarization plane within the analyzer setup. The Mueller matrix for this system of optics is

$$\mathbf{A}\left(\frac{\Gamma_{\text{wp}}}{2}\right) = \mathbf{P}(0)\mathbf{V}(\Gamma_{\text{wp}}, 45^\circ)\mathbf{Q}(0),$$

$$= \frac{1}{2} \begin{bmatrix} 1 & \cos\Gamma_{\text{wp}} & \sin\Gamma_{\text{wp}} & 0 \\ 1 & \cos\Gamma_{\text{wp}} & \sin\Gamma_{\text{wp}} & 0 \\ 0 & 0 & 0 & 0 \\ 0 & 0 & 0 & 0 \end{bmatrix}, \quad (15)$$

where Γ_{wp} is the voltage-controlled phase shift of the LCVR. This allows the polarizer to select any linear polarization component by adjusting Γ . The Mueller matrix in Eq. (15) differs from a rotated linear polarizer because the output polarization is always horizontal. This property is a result of CAPABL's specific setup. The single output polarization means all optics after the analyzer always experience the same polarization. Thus, the measurements are only dependent on the intensity of the observed signal. The polarization effects of the optical components after the analyzer do not impact the accuracy of CAPABL.

Accurate alignment of CAPABL's polarization analyzer is necessary to obtain the high polarization accuracy required for diattenuation measurements of HOIC. For this reason, particular attention is given to the alignment of the QWP, LCVR, and polarizer that make up the polarization analyzer in the receiver to which all other components must be aligned. Clear-sky observations have demonstrated that the minimum linear depolarization ratio observable by CAPABL is 0.025. This value may be interpreted as the error (maximum resolution) of CAPABL's polarization measurements due to the polarization effects of the instrument.

a. Accuracy of observed polarizations

The LCVR imposes a voltage-controlled phase shift to change the observed polarization mode. However, the phase shift created in the optical medium of the LCVR drifts as a function of temperature. CAPABL is contained in a temperature-controlled room at Summit, but some temperature drift does occur in the room. A sensitivity analysis of diattenuation measurements for a relative phase shift error of $\Delta\Gamma_{\text{wp}}$ was performed. For a depolarizing medium described by Eq. (2), the received photon counts as a function of phase shift on the LCVR are given by

$$N_{\text{RX}}(\Gamma_{\text{wp}}) = \frac{N_0}{2} [f_{11} - f_{22} \sin\Gamma_{\text{wp}}], \quad (16)$$

where N_{RX} are the photons detected, N_0 are the photons incident on the LCVR, f_{22} is the (2,2) element of the scattering matrix describing axially symmetric randomly oriented scatterers from Eq. (2), and Γ_{wp} is the phase shift of the LCVR.

The objective of diattenuation measurements with CAPABL is to identify oriented scatterers. Thus, the primary concern is avoiding false positives (i.e., nonzero diattenuation due to a systemic effect) in the presence of strictly randomly oriented scatterers. Because the room where CAPABL operates is heated through standard heating, ventilation, and air-conditioning (HVAC) systems, the LCVR retardance error is generally small. The received photon counts for a Γ_{wp} and $\Delta\Gamma_{\text{wp}}$ is expanded from Eq. (16) to first order,

$$N_{\text{RX}}(\Gamma_{\text{wp}}) \approx \frac{N_0}{2} (f_{11} - f_{22} \sin\Gamma_{\text{wp}}) - \frac{N_0}{2} f_{22} (\cos\Gamma_{\text{wp}}) \Delta\Gamma_{\text{wp}}. \quad (17)$$

Here, the second term corresponds to error in the detected photon counts. The first-order error sensitivity of the perpendicular and parallel photon counts [at $\Gamma_{\text{wp}} = -(\pi/2)$ and $\Gamma_{\text{wp}} = \pi/2$, respectively] is zero. Higher-order terms are always equal and opposite between $-(\pi/2)$ and $\pi/2$, and because two terms are summed in diattenuation calculations, the error terms cancel. Thus, diattenuation measurements are relatively insensitive to LCVR phase error in the perpendicular and parallel measurements. To maintain accurate phase shifts corresponding to perpendicular and parallel polarizations, only periodic recalibration of the LCVR voltage settings is required.

The 45° polarization measurement is made at $\Gamma_{\text{wp}} = 0$, where Eq. (17) has maximum sensitivity to $\Delta\Gamma_{\text{wp}}$. The measured diattenuation of the randomly oriented scatterers as a function of LCVR error in the 45° plane is given by evaluating Eq. (7) with Eq. (11) at each corresponding phase shift, resulting in

$$D_q = -f_{22} \Delta\Gamma_{\text{wp}}. \quad (18)$$

Because randomly oriented scatterers are only being considered in this analysis, any nonzero value of D_q must be strictly related to the error. Deviations from zero may therefore be used to determine the phase error of the LCVR. This error is then used in a feedback loop to control the LCVR voltage for 45° polarization measurements.

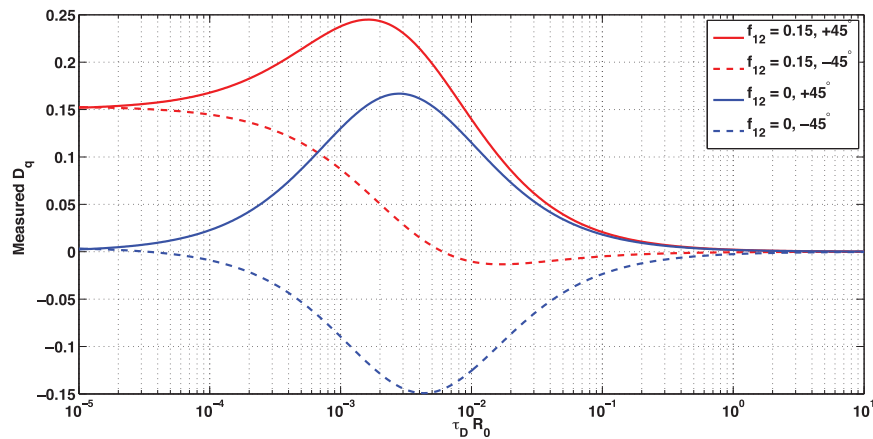


FIG. 5. Measured diattenuation when calculated using 45° (solid) and -45° (dashed) polarization measurements as a function of detector saturation when the atmosphere exhibits no diattenuation (blue) and when it exhibits a diattenuation of 0.15 (red). Nonlinear response on the detectors causes the two calculations to diverge, but the atmospheric effect produces a bias. Opposite signs in the diattenuation measurements are considered an indicator of artificially induced diattenuation, not attributable to oriented ice crystals.

The feedback loop for the LCVR control is closed using part of the lidar profile. However, to make precise corrections to the LCVR voltage, the uncertainty from the signal-to-noise requirements of the photon counts must be low and we must assume that this part of the profile contains no actual diattenuating particles. Therefore, low-altitude signals, where photon counts are high, are used to close the feedback loop. To obtain a diattenuation uncertainty of less than 1% from the feedback signal, individual profiles are further integrated in the feedback loop. Longer integration has the effect of reducing the control bandwidth but since phase shift drift caused by temperature fluctuations is slow, the controller bandwidth is only a concern with regard to settling time when first starting the loop. Currently, the feedback loop takes 10–20 min from start-up to lock on the appropriate value of Γ_{wp} . After the loop has settled on this value, its time response is able to react quickly enough to normal operational changes in building temperature to adapt Γ_{wp} during the duration of the measurement without corrupting the observations.

b. Nonlinear photon counting

Nonlinear photon counting due to detector saturation is also a large concern for the depolarization and diattenuation measurements, as these are functions of the parallel channel photon counts [Eqs. (4), (7), and (8); Donovan et al. 1993; Liu et al. 2009]. It should be noted that the impact of saturation is not unique to this method and may have an especially large impact on observations that attempt to identify HOIC by high specular backscatter

and low depolarization (Sassen et al. 2003; Hu et al. 2009; Sassen 2005; Noel and Chepfer 2010). To verify CAPABL's diattenuation measurement, a fourth polarization measurement was added in November 2011 to identify the effects of detector saturation of the \mathcal{F}_{12} term.

The equations used to derive the polarization properties of the scatterer problem assume that the recorded signals are linearly proportional to the backscattered intensity. Nonlinearity in the recorded signal results in erroneous polarization measurements and presents a major concern in using nonzero diattenuation to detect ice crystal orientation. Though CAPABL uses only one detector for all three polarization measurements, their relative signal levels can be different by up to two orders of magnitude. We assume the photon counting of the system is nonparalyzable, so the detected photon count rate is related to the actual count rate through

$$R_d = \frac{R_0}{1 + \tau_D R_0}, \quad (19)$$

where R_d is the detected photon count rate, R_0 is the actual photon arrival rate, and τ_D is the discriminator dead time of the data acquisition system (Donovan et al. 1993; Liu et al. 2009). When the response of the parallel signal is less than that of the other two measurements, the diattenuation will drift positive, even when no such behavior is exhibited by the atmosphere.

The atmospheric diattenuation can also be calculated by measuring the backscattered signal at an arbitrary

$\Gamma_{wp}(\pi/2 < |\Gamma_{wp}| < \pi)$; here, we use -45° as an example. In that case Eq. (7) is slightly modified to reflect the change sign to

$$D_q^{(-45)} = 1 - \frac{2N_{-45}}{N_{\parallel} + N_{\perp}}. \quad (20)$$

As opposed to the previously introduced measurement of Eq. (6), this signal will drift negative as the parallel channel begins to saturate. Figure 5 shows the measured diattenuation using the positive and negative 45° polarization measurements as a function of the detector saturation when the atmosphere has a diattenuation of 0.15 and when it has no diattenuation. If saturation is occurring, then the two channels drift opposite of each other; however, when the diattenuation is real, the bias prevents the -45° measurement from crossing zero. When there is no saturation, both calculations produce the same diattenuation value. This relationship provides a filter and diagnostic for saturation in the measurement set.

During CAPABL's initial operation, it was impossible to rule out the contributions of detector nonlinearity to profiles demonstrating diattenuation. CAPABL obtains parallel, perpendicular, and 45° measurements using $\Gamma_{wp} = (-\pi)/2, 0, \pi/2$, respectively (where $\mathcal{F}_{33} < 0$). In November of 2011, a fourth polarization measurement, at an arbitrary $\Gamma_{wp}(\pi/2 < |\Gamma_{wp}| < \pi)$, was added to CAPABL to discern between actual diattenuation signals and observations biased by detector saturation. When the calculated diattenuation is the same on the 45° and fourth channels, the diattenuation signal may be reasonably attributed to an atmospheric polarization effect. When the signals show opposite signs, the signal is assumed to be the result of detector nonlinearity.

A secondary issue relating to detector nonlinearity arises when low-altitude stratus clouds are present. These events result in very high backscatter levels at low altitudes as well as high extinction, so backscatter data cannot be retrieved above such clouds. In these cases, saturation effects corrupt the feedback signal of the LCVR controller. When this happens, the feedback loop controls the profile to cancel the apparent positive diattenuation induced by detector nonlinearity. An attempt has been made to turn off the feedback loop when diattenuation is present in low-altitude clouds and corrupts the feedback signal. However, drift in the LCVR phase shift can occur and it is difficult to support findings of oriented scatterers under these conditions. For this reason, diattenuation data are generally ignored when the feedback signals are corrupted by saturation and where no clear zero diattenuation baseline exists in the observed profile.

6. Backscatter retrieval

CAPABL also provides traditional lidar backscatter ratio observations associated with the presence of clouds and aerosols. CAPABL uses the retrieval method for aerosol backscatter originally employed and described by Fernald et al. (1972) and Klett (1981). This method is in wide use, and the results of this previous work is only paraphrased here to explicitly describe the method employed for this lidar (Russell et al. 1979; Fernald 1984; Thayer et al. 1997; Hofmann et al. 2003; Pappalardo et al. 2004).

The backscatter ratio is defined as the ratio of the total backscatter coefficient to the molecular backscattering coefficient. Physically, the lidar backscatter ratio R is defined as

$$R(z) = \frac{\beta_a(z) + \beta_m(z)}{\beta_m(z)}, \quad (21)$$

where $\beta_a(z)$ and $\beta_m(z)$ are the aerosol and molecular backscatter coefficients, respectively. The molecular backscatter is calculated from temperature and pressure profiles obtained twice daily from collocated radiosonde launches. The scattering ratio is calculated by evaluating

$$R(z) = \frac{CS(z)z^2}{\beta_m(z)T^2(z)}, \quad (22)$$

where $S(z)$ is the background subtracted lidar signal, $T^2(z)$ is the two-way atmospheric transmittance, and C is a system constant determined by normalizing the right-hand side of the equation to an expected minimum value of R over a specified altitude range.

For CAPABL, extinction measurements from the Optical Spectrograph and Infrared Imager System (OSIRIS) aboard the *Odin* spacecraft were used to constrain the minimum R value in the calibration region (Bourassa et al. 2011). This was done by converting the observed OSIRIS extinction to R during periods when both OSIRIS and CAPABL coincidentally observed clear-sky above Summit (within 5°). Values of R were obtained at these times at the highest altitude to which CAPABL observed photon counts with signal-to-noise errors less than 5% (Ansmann et al. 1992; Jäger and Deshler 2002, 2003). This process was performed several times in different seasons, and seasonally averaged R values are applied to the dataset to derive the R for all observations (Ansmann et al. 1992). As observations continue, this process will be repeated to help reduce error in the derived R . A geometric overlap correction (up to a range of 200 m) is also applied to aerosol

backscatter data products based on obtaining a backscatter ratio of unity during a very clean-air episode. The overlap correction is not needed for HOIC detection because the retrieval is only a ratio of the separate polarization signals, which is impacted by the overlap region equally.

The transmittance is calculated from a combination of a radiosonde-derived molecular extinction model, lidar-derived aerosol extinction, and modeled ozone absorption. During periods of moderate to heavy aerosol loading, aerosol extinction must be scaled to the aerosol backscatter (Jäger and Deshler 2002). Under background conditions in the stratosphere, it can be ignored. Equation (17) is then solved iteratively from the top of the profile down, using an updated value of aerosol extinction for each iteration.

7. Example observations

A set of example observations made on 15 November 2010 (zenith pointing), 18 February 2012 (11° tilt), and 8 February 2012 (11° tilt) are shown in Figs. 6–11 (all observations are shown with heights relative to the elevation of Summit Station, i.e., above the surface). The observations shown here serve as an example of CAPABL's technical observational ability.

Figure 6a shows δ , R (Fig. 6c), and their associated error terms (Figs. 6b and 6e) with a vertical resolution of 30 m and a temporal resolution of 110 s for 15 November 2010. This day included several cloud systems with precipitating snow and ice with a period of clear air in the middle of the day. Figure 6d is the corresponding radar reflectivity collect by the collocated Doppler, 35-GHz, millimeter cloud radar (MMCR) (Shupe et al. 2013). Figure 6e is an estimate of the OD due to the liquid water path (LWP) derived from observations made by a Humidity and Temperature Profiler (HATPRO, a microwave radiometer) and a high-frequency microwave radiometer (MWRHF) assuming an effective radius of 10 μm (Stephens 1978; Shupe et al. 2013). The OD value reported here does not include ice and should only be considered a lower bound of the total OD. Because the optical depth value is directly proportional to the LWP, it is also useful for a relative comparison to the phase classification indicated by δ . The MWRHF is able to measure LWP to an accuracy of $\sim 3 \text{ g m}^{-2}$, which when combined with an assumed effective radius of 10 μm translates into an optical depth of 0.5. Thus, the majority of the cases where OD is less than 0.5 is in actuality liquid-water-free conditions. Figure 7 depicts the corresponding temperature and humidity profiles collected by radiosonde launches at Summit during this day.

Of particular note during this day is a multilevel cloud system beginning at ~ 1700 UTC. In this instance CAPABL is able to discern between a liquid cloud layer at ~ 750 m and light ice precipitating above the layer and strong ice precipitation below the layer. The distinction between a liquid layer and ice precipitation is made by comparing δ with the R in a manner similar to previous work (Sassen 1992). Liquid water is characterized by high backscatter and low δ , while the ice has relatively lower R and much higher δ . The color threshold in the volume linear depolarization scale for Figs. 6, 8, and 11 is set at a value of 0.08. This helps draw a definitive line between volumes containing a majority of scatters of pure liquid (spheres) and a majority of scatterers containing ice (nonspherical scatterers).

The higher-level ice cloud and precipitation is corroborated by the radar observation. The increase in OD due to the LWP at ~ 1700 UTC confirms the liquid layer identified by CAPABL. Similarly, the feature from ~ 0800 to 1000 UTC is a surface liquid cloud with high LWP OD. The cloud is not seen in Fig. 6d because it is below the lowest level of detection for the radar. When the cloud rises above 100 m, CAPABL is clearly able to identify a liquid layer. This is confirmed by the large LWP OD during this period. During the rest of the day, the atmosphere is dominated by periods of mixed-phase clouds, regions of high δ , and clear sky.

On 18 February 2012 (Fig. 8), CAPABL observed two diattenuation signatures (magenta circles 1 and 2) that coincided with clouds at altitudes between 3000 and 4500 m from 0230 to 0530 UTC for circle 1 and between 1000 and 2500 m from 0500 to 0630 UTC for circle 2. During this same period, signals at lower altitudes depict variable linear depolarization with no concomitant diattenuation. Figure 9 depicts the corresponding temperature profiles for this day.

Because nonlinear photon counting can produce false diattenuation features, saturated three-channel measurements can easily be misinterpreted as evidence of ice crystal orientation. Because of the receiver's inability to linearly count photons at three widely varying intensities, the saturation effect is not constant and does not simply cancel out of Eq. (7). Integrated profiles from diattenuation event 2, derived using the 45° and fourth polarization channels separately, are shown in Fig. 10. The period of integration (0530–0600 UTC) is denoted as region 3 in Fig. 8. The two diattenuation profiles demonstrate how CAPABL's separate measurements help determine the difference between false-positive diattenuation due to detector saturation and actual variations in diattenuation. The region from 1200 to 2500 m, where both diattenuation profiles have a value of ~ -0.1 , which is well above the error limits denoted in red,

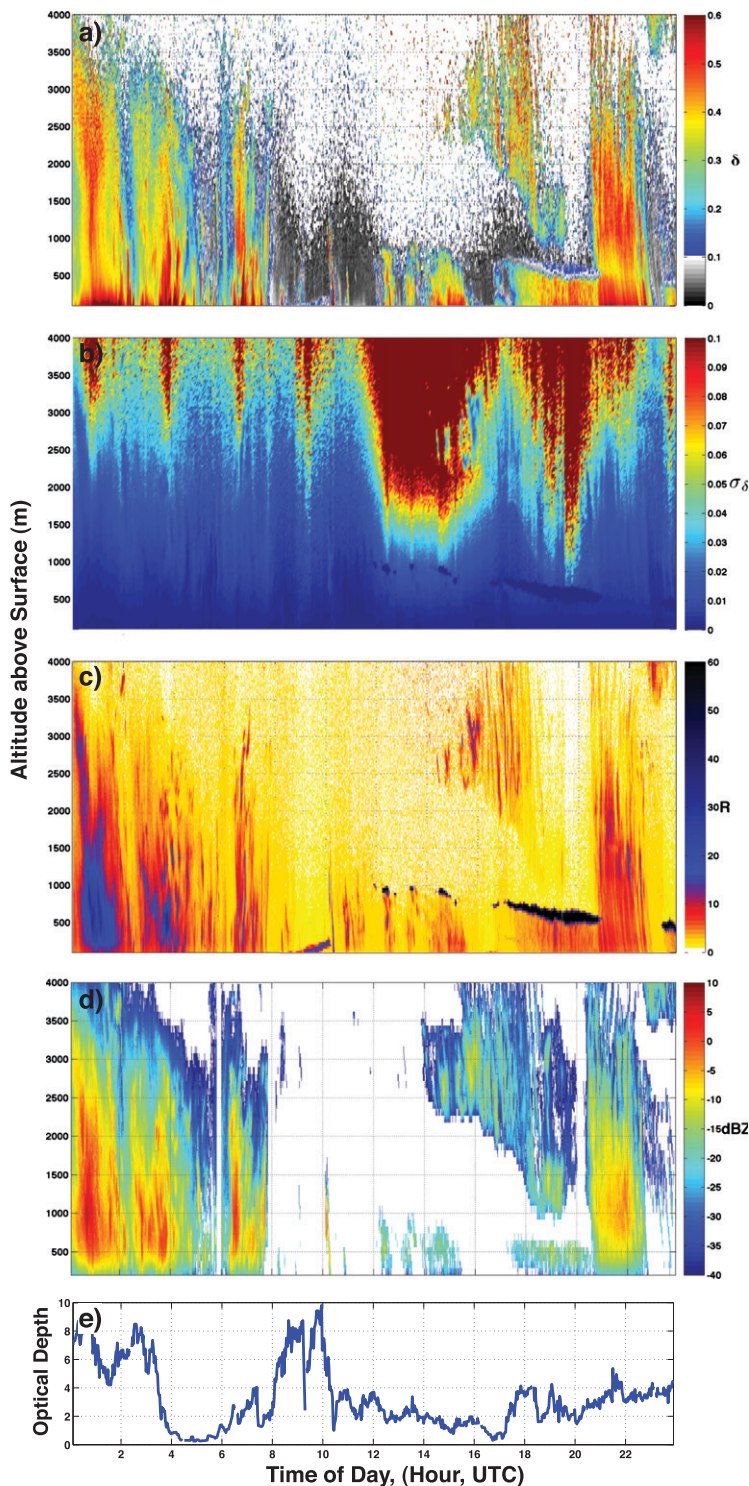


FIG. 6. Example observation made on 15 Nov 2010 of (a) δ , [with (b) the associated relative error] and (c) R . Concurrent (d) radar observations and (e) LWP OD. Observations made by CAPABL (while pointing near zenith) are shown with a vertical resolution of 30 m and a temporal resolution of 110 s. Shown are (a)–(d) plotted as altitude above the surface of Summit (3200 MSL) vs hour of day (UTC); and (e) depicts the total LWP OD (unitless vertical axis) vs time.

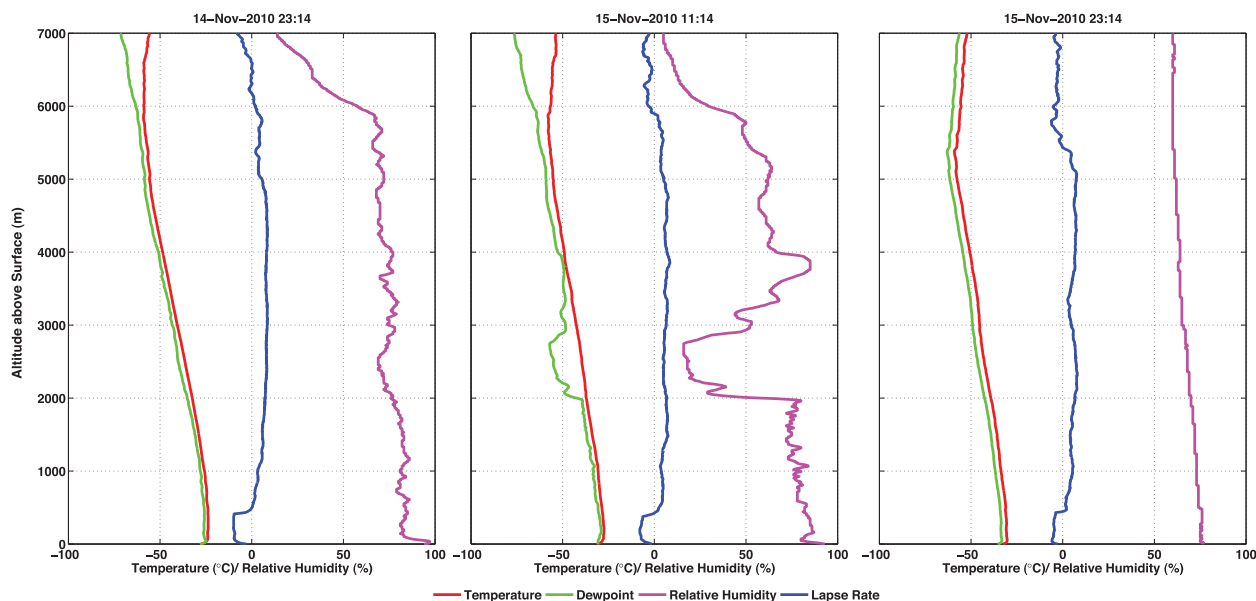


FIG. 7. Temperature and humidity profiles observed by radiosondes at approximately 0000 and 1200 UTC 15 Nov 2010 and 0000 UTC 16 Nov 2010. Actual launch time of the sonde is labeled at the top of each panel.

confirm that the detection of diattenuating scatterers is an atmospheric effect rather than a systemic bias. Regions where the two diattenuation profiles behave oppositely, as is seen in the bottom of the profile, are due to detector saturation as described above (Fig. 5).

The right panel of Fig. 10 confirms that the photon count rate of the diattenuating region 2 is ~ 1.5 orders of magnitude lower than count rates observed near the surface, where impacts of detector nonlinearity are detected. Therefore, it is unlikely that detector nonlinearity is responsible for the diattenuation signature observed. It should be noted that this method of determining the impacts of detector nonlinearity on the observation, using the additional diattenuation assessment, is preferable to setting an arbitrary limit on the observed photon count rate. Arbitrary count rates could easily lead to a misclassification of diattenuation events, while the method described here provides a robust test of the impact of detector saturation for all ranges of photon counts. This is further demonstrated in Figs. 11–13.

An example of an identification of a false-positive diattenuation event on 8 February 2012 is given in Fig. 11. Corresponding temperature profiles from this day are shown in Fig. 12 and an integrated set of profiles, analogous to Fig. 10, are found in Fig. 13. Without the secondary assessment of diattenuation, Figs. 11 and 13 depict a convincing nonzero diattenuation event occurring from 0100 to 0300 UTC along the lower boundary of cloud descending from 1000 to 700 m; the photon count

rate (right panel of Fig. 13) is not conclusively higher than the linear range. Using only the three-channel measurements, it would be concluded that the event from 0100 to 0300 UTC was indicative of atmospheric diattenuation peaking at 800 m (left panel of Fig. 13); the photon count rate is not conclusively higher than the linear range (right panel of Fig. 13). This leaves the uncomfortable question of arbitrarily characterizing the event as saturation, atmospheric diattenuation, or possibly both. However, inspection of the fourth-channel-derived diattenuation shows that it is anticorrelated in the region of interest without any asymmetric properties, indicating it is a saturation event. This demonstrates full usefulness and sensitivity of including the fourth channel in the measurement technique. This also demonstrates the method whereby the validity of the diattenuation observations is determined without requiring arbitrary bounds on the instrument's dynamic range.

This set of observation provides a demonstration of operationally detecting diattenuation signals that are indicative of HOIC by direct polarization determination. Furthermore, CAPABL can simultaneously determine the cloud phase of randomly oriented scatterers and assess the variation in the diattenuation of the scatterers, which may be used to interpret the presence of HOIC. The measurements presented in Figs. 6, 8, and 11 illustrate the benefits of a multipolarization channel lidar in studying polar atmospheric processes, particularly those involving the phase of water.

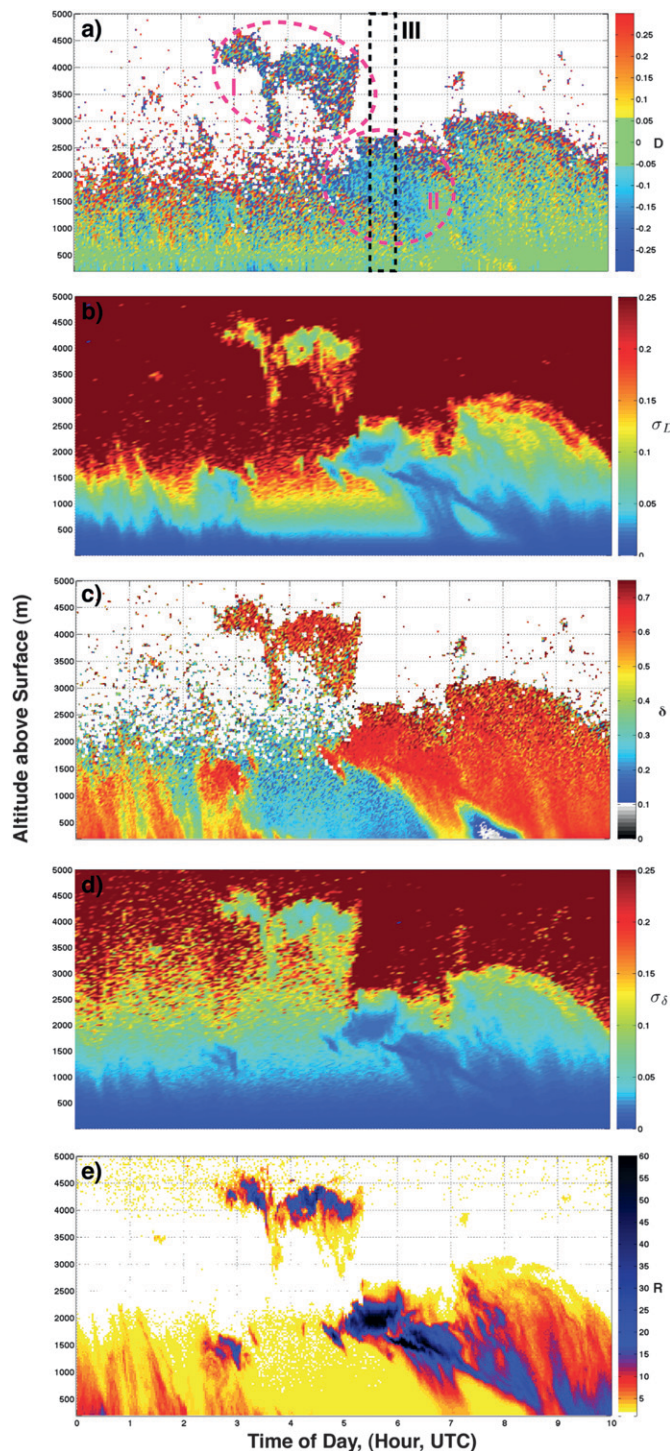


FIG. 8. Example observation made on 18 Feb 2012 of two diattenuation events: (a) D with (b) the associated relative error, and (c) δ with (d) the associated relative error and (e) R . During this observation the lidar was pointing at 11° with a vertical resolution of 30 m, a temporal resolution of 110 s, and the data were plotted with altitude referenced from the surface of Summit (3200 m MSL). A threshold of ± 0.05 was set for the diattenuation plot to help distinguish the HOIC event from non-diattenuating signals and noise.

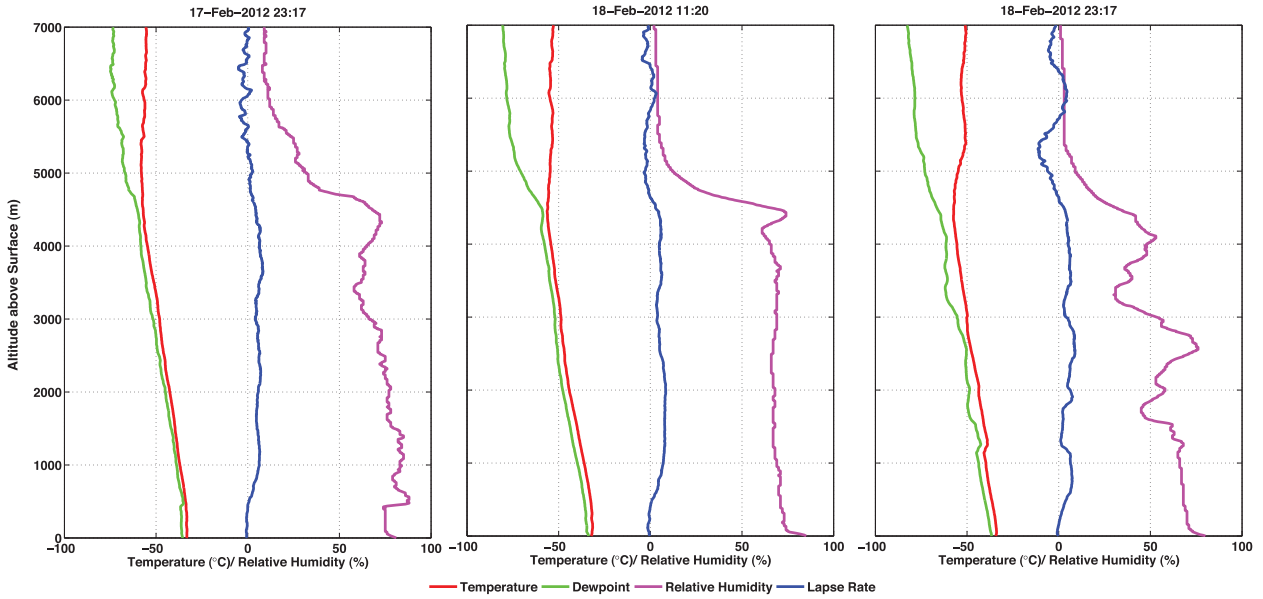


FIG. 9. Temperature and humidity profiles observed by radiosondes at approximately 0000 and 1200 UTC 18 Feb 2012 and 0000 UTC 19 Feb 2010. Actual launch time of the sonde is labeled at the top of each panel.

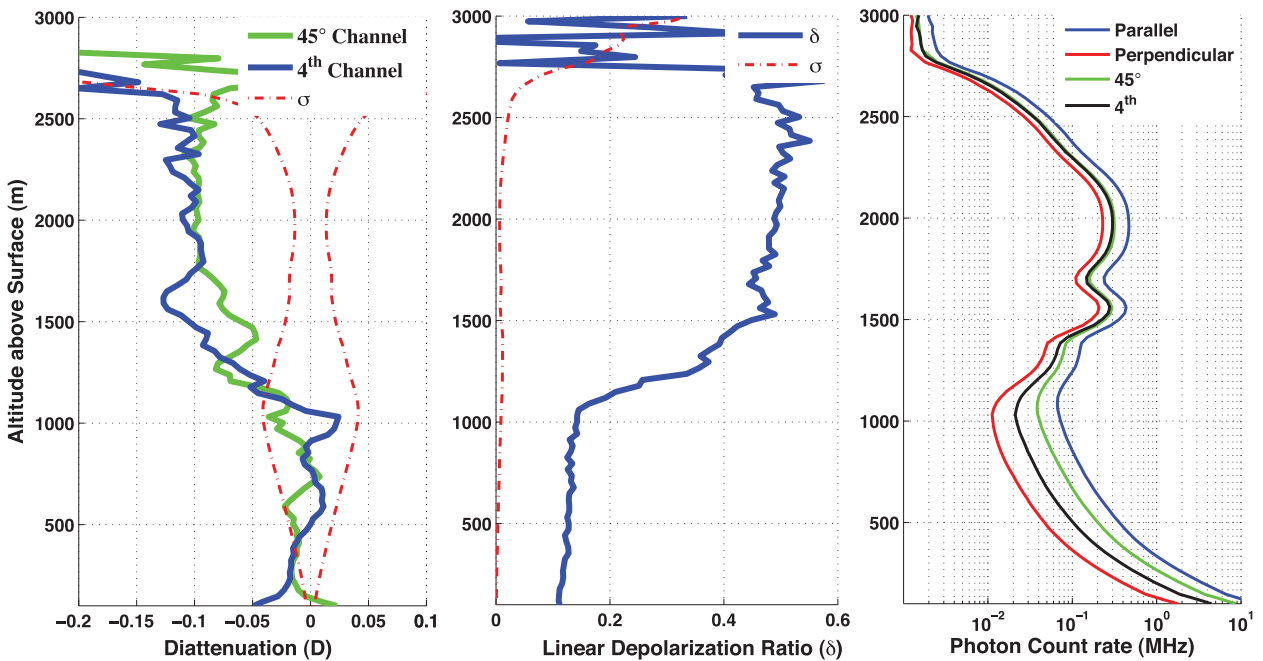


FIG. 10. Time-integrated profile (30-m vertical resolution) of an actual HOIC event from 0530 to 0600 UTC 18 Feb 2012 (region 3 in Fig. 8a). (left) Diattenuation calculated from the 45° channel and the fourth channel. (center) Volume linear depolarization observation made simultaneously with the diattenuation measurements. Dashed lines represent the error associated with each derived observation obtained through standard propagation of error techniques of the signal-to-noise error associated with the observation from each polarization. (right and center) Photon count rates of each polarization channel during this period.

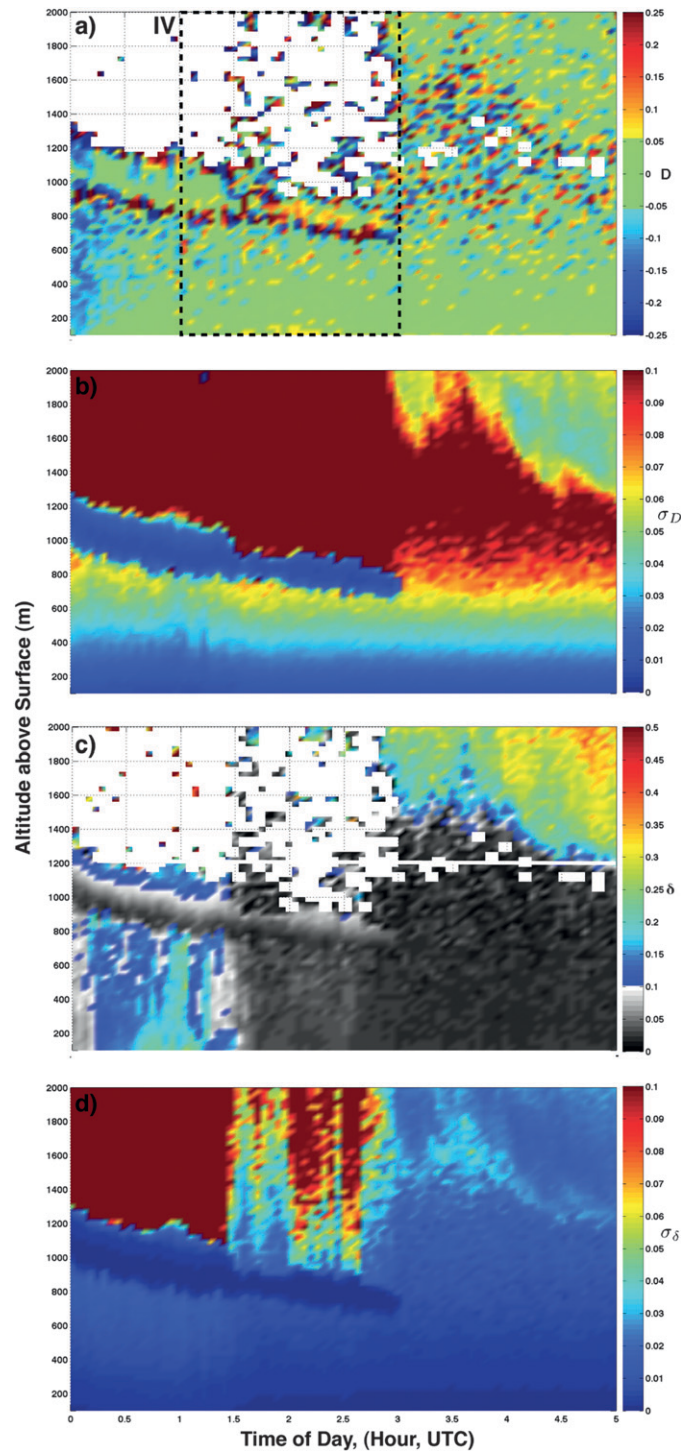


FIG. 11. Example observation of a false diattenuation event caused by the nonlinear response of the detector made on 8 Feb 2012. Parameters shown include (a) D_g , with (b) the associated relative error, (c) δ , with (d) associated relative error. For this observation the lidar is pointing at 11° , the vertical resolution is 30 m, the temporal resolution is 110 s, and the data are plotted with altitude referenced from the surface of Summit (3200 m MSL). As in Fig. 8, a threshold at ± 0.05 was set for the diattenuation plot to help distinguish the HOIC event from non-diattenuating signals and noise.

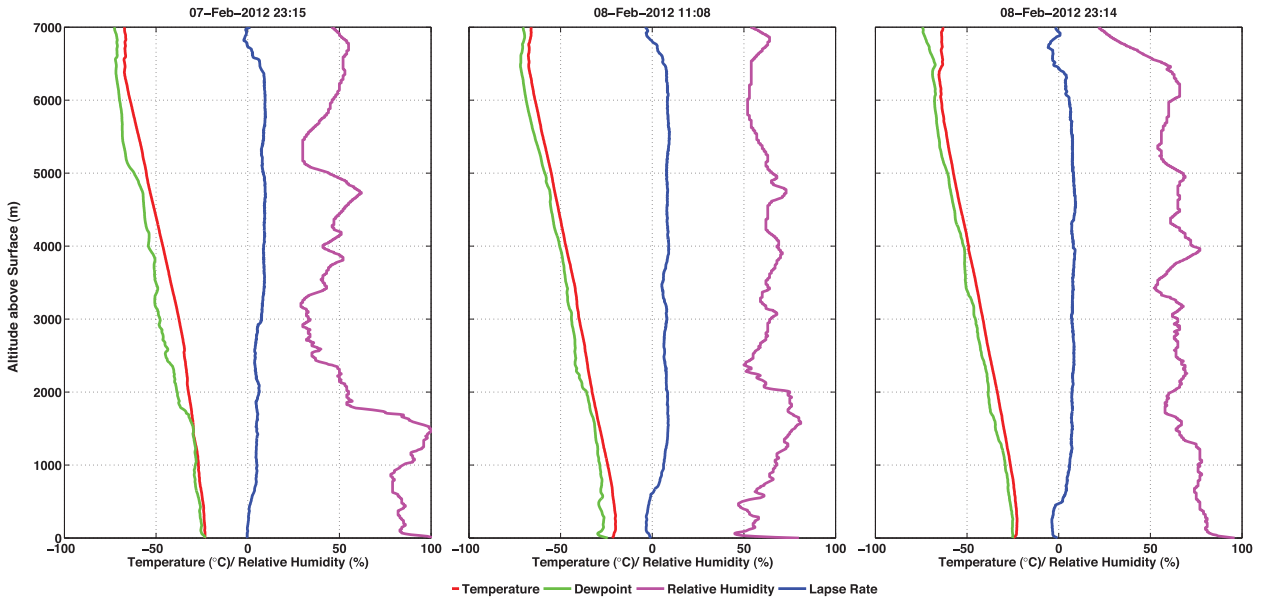


FIG. 12. Temperature and humidity profiles observed by radiosondes at approximately 0000 and 1200 UTC 8 Feb 2012 and 0000 UTC 9 Feb 2010. Actual launch time of the sonde is labeled at the top of each panel.

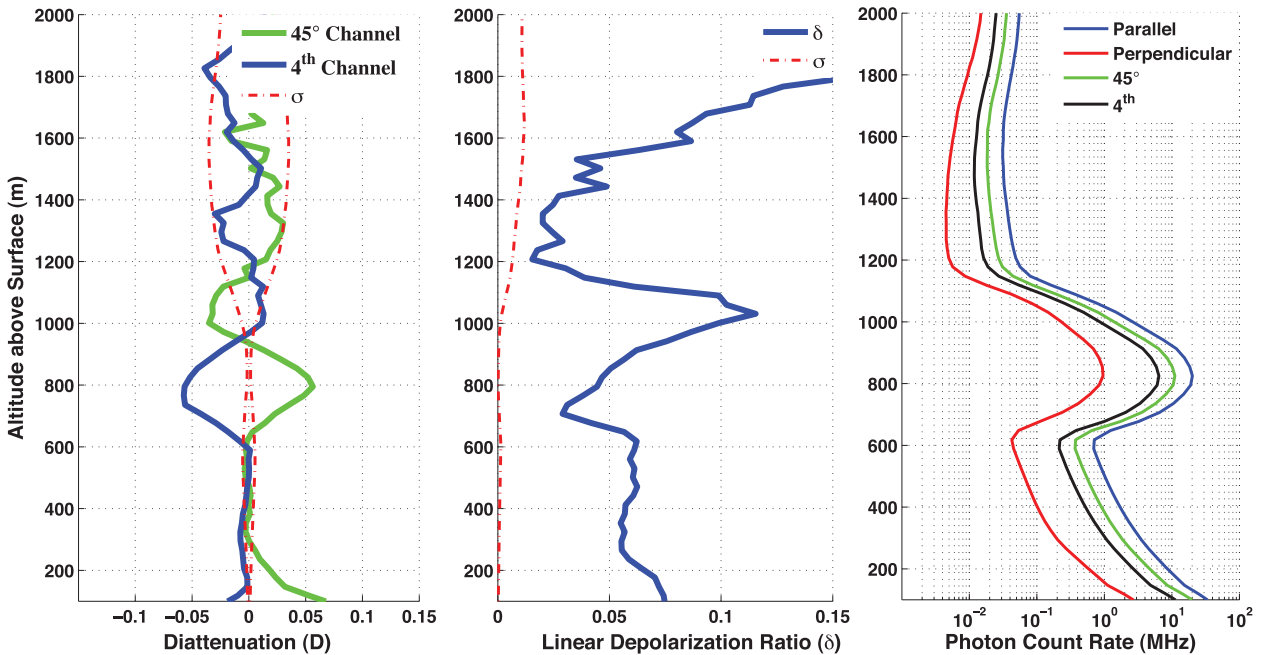


FIG. 13. Time-integrated profile (30-m vertical resolution) that contains a false diattenuation signal cause by detector saturation from 0100 to 0300 UTC 8 Feb 2012 (region 4 in Fig. 11a). (left) Diattenuation calculated from the 45° channel and the fourth channel. (center) Volume linear depolarization observation made simultaneously with the diattenuation measurements. Dashed lines represent the error associated with each derived observation obtained through standard propagation of error techniques of the signal-to-noise error associated with the observation from each polarization. (right and center) Photon count rates of each polarization channel during this period.

8. Summary

Recent rapid melting of Arctic sea ice is likely influenced by changes in cloud cover, radiation, and circulation (Francis and Hunter 2006; Kay et al. 2008; van den Broeke et al. 2009; Shupe et al. 2011). Signatures of climate change are known to be most evident in the polar regions (Washington and Meehl 1989). Thus, it is not surprising that concurrent with the dramatic sea ice losses, the GIS is experiencing similar rapid melting (Rignot and Kanagaratnam 2006). Detailed information on cloud amount and type is needed to accurately determine the effect of climate change on snowmelt by using energy balance in global climate models (Cawkwell and Bamber 2002). Many shortcomings in numerical models are likely caused by unrealistic assumptions or parameterizations of cloudiness due to a shortage of observations over the GIS (Cawkwell and Bamber 2002). Accurate measurements of atmospheric aerosols, especially the determination of the thermodynamic phase of hydrometeors, are essential to further our understanding of the effects of clouds and aerosols on the radiative budget of the GIS.

CAPABL uses recent advances in lidar polarization theory (Hayman and Thayer 2012) to develop techniques that better identify the information needed to help understand the microphysical properties of clouds and how these properties are changing climatically over the GIS. Observations indicate that CAPABL can accurately determine altitude profiles at high spatial and temporal resolution of the aerosol backscatter ratio, the linear depolarization ratio, and a new data product called linear diattenuation through the combination of three polarization channels. Through careful configuration of the lidar system, polarization effects of the system are minimized, and errors in depolarization and diattenuation estimates are below a few percent and primarily limited by photon-counting statistics. The first observations of diattenuation in atmospheric scatters are demonstrated and show promise in unequivocal detection of horizontally oriented ice crystals. CAPABL incorporates self-verification of atmospheric diattenuation by incorporating a fourth polarization channel to check against false-positive diattenuation detection due to detector saturation. This ability has also been used, when no diattenuation is present, to access the impact of saturation in other observations.

In this work we have described the need, theory, and implementation of hardware to reliably measure diattenuation with CAPABL. This has ensured confidence that detection of a nonzero diattenuation signature is attributable to atmospheric scatterers, not systemic effects. The data shown here demonstrate CAPABL's

ability to detect polarization signatures that may be used to assess the occurrence of HOIC. A successful campaign of detecting HOIC can have broad implications for our understanding of the radiative budget. HOIC lead to increased cloud albedo, which leads to a proportional reduction in the surface solar flux (Sassen et al. 2003). Thus, an accurate long-term record of the occurrence of HOIC, in conjunction with the full array of cloud parameters collected by ICECAPS, is needed to understand the consequences orientation may have on the heating of the atmosphere and the surface. Also, HOIC, when scattering normal to its surface, can exhibit low linear depolarization ratios that can result in erroneous classification of the thermodynamic phase. Diattenuation measurement enables lidar systems to detect oriented scatterers within the same dynamic range as other cloud signals. This new observational method therefore allows for an easier and more certain means of collecting comprehensive observations of clouds and oriented particles.

Acknowledgments. This material is based upon work supported by the National Science Foundation (NSF) under Grants ATM-0454999 and ARC-0856559, and the National Center for Atmospheric Research. The research done by Ryan R. Neely III was supported by the ESRL-CIRES Graduate Research Fellowship. Robert Stillwell was funded by the University of Colorado at Boulder Undergraduate Research Opportunities Program Individual Grant Fund. We thank NOAA's Earth System Research Laboratory's Chemical Science Division, whose original work on DABUL made CAPABL possible, including Dr. Wynn Eberhard, Dr. Raul Alverez, Dr. Richard Marchbanks, Scott Sandberg, Dr. Alan Brewer, and Dr. Christoph Senff. The authors also thank the entire ICECAPS team, especially the vision and hard work of the additional PI's of the ICECAPS project, Dr. Von Walden, Dr. David Turner, and their graduate students, particularly Chris Cox, who helped to provide the estimate of optical depth from the P-AERI.

REFERENCES

- Alvarez, R., W. Eberhard, J. Intrieri, S. P. Sandberg, and K. W. Koenig, 1998: Cloud backscatter and phase measurements in the Arctic using ETL's DABUL lidar. Preprints, *Fourth Int. Symp. on Tropospheric Profiling*, Boston, MA, Amer. Meteor. Soc., 7–9.
- Ansmann, A., U. Wandinger, M. Riebesell, C. Weitkamp, and W. Michaelis, 1992: Independent measurement of extinction and backscatter profiles in cirrus clouds by using a combined Raman elastic-backscatter lidar. *Appl. Opt.*, **31**, 7113–7131.
- Bailey, M., 2009: A comprehensive habit diagram for atmospheric ice crystals: Confirmation from the laboratory, AIRS II, and other field studies. *J. Atmos. Sci.*, **66**, 2888–2899.

- Barnes, J., and D. Hofmann, 1997: Lidar measurements of stratospheric aerosol over Mauna Loa Observatory. *Geophys. Res. Lett.*, **24**, 1923–1926.
- Borys, R., D. Del Vecchio, J.-L. Jaffrezo, C. Davidson, and D. Mitchell, 1993: Assessment of ice particle growth processes at dye-3, Greenland. *Atmos. Environ.*, **27A**, 2815–2822.
- Bourassa, A., L. Rieger, N. Lloyd, and D. A. Degenstein, 2011: Odin-OSIRIS stratospheric aerosol data product and SAGE III intercomparison. *Atmos. Chem. Phys. Discuss.*, **11**, 25 785–25 811.
- Cawkwell, F., and J. Bamber, 2002: The impact of cloud cover on the net radiation budget of the Greenland Ice Sheet. *Ann. Glaciol.*, **34**, 141–149.
- Chepfer, H., and G. Brogniez, 1998: Cirrus clouds' microphysical properties deduced from POLDER observations. *J. Quant. Spectrosc. Radiat. Transfer*, **60**, 375–390.
- Donovan, D. P., J. A. Whiteway, and A. I. Carswell, 1993: Correction for nonlinear photon-counting effects in lidar systems. *Appl. Opt.*, **32**, 6742–6753.
- Fernald, F. G., 1984: Analysis of atmospheric lidar observation:—Some comments. *Appl. Opt.*, **23**, 652–653.
- , B. M. Herman, and J. A. Reagan, 1972: Determination of aerosol height distributions by lidar. *J. Appl. Meteor.*, **11**, 482–489.
- Flynn, C. J., A. Mendoza, Y. Zheng, and S. Mathur, 2007: Novel polarization-sensitive micropulse lidar measurement technique. *Opt. Express*, **15**, 2785–2790.
- Francis, J. A., and E. Hunter, 2006: New insight into the disappearing Arctic sea ice. *Eos, Trans. Amer. Geophys. Union*, **87**, 509–511.
- Gimmestad, G. G., 2008: Reexamination of depolarization in lidar measurements. *Appl. Opt.*, **47**, 3795–3802.
- Griggs, J., and J. Bamber, 2008: Assessment of cloud cover characteristics in satellite datasets and reanalysis products for Greenland. *J. Climate*, **21**, 1837–1849.
- Hansen, J., M. Sato, P. Kharecha, and K. von Schuckmann, 2011: Earth's energy imbalance and implications. *Atmos. Chem. Phys. Discuss.*, **11**, 27 031–27 105.
- Hayman, M., 2011: Optical theory for the advancement of polarization lidar. Ph.D. thesis, University of Colorado, 201 pp.
- , and J. P. Thayer, 2009: Accounting for system affects in depolarization lidar. *Proc. Int. Quantum Electronics Conf.*, Baltimore, MD, Lasers and Electro-Optics Society, JTuD86. [Available online at <http://www.opticsinfobase.org/abstract.cfm?URI=IQEC-2009-JTuD86>.]
- , and —, 2012: General description of polarization in lidar using Stokes vectors and polar decomposition of Mueller matrices. *J. Opt. Soc. Amer.*, **29A**, 400–409.
- Hofmann, D., J. Barnes, E. Dutton, T. Deshler, H. Jäger, R. Keen, and M. Osborn, 2003: *Surface-Based Observations of Volcanic Emissions to the Stratosphere*. *Geophys. Monogr.*, Vol. 139, Amer. Geophys. Union, 57–73.
- , —, M. O'Neill, M. Trudeau, and R. Neely, 2009: Increase in background stratospheric aerosol observed with lidar at Mauna Loa Observatory and Boulder, Colorado. *Geophys. Res. Lett.*, **36**, L15808, doi:10.1029/2009GL039008.
- Hu, Y., and Coauthors, 2009: CALIPSO/CALIOP cloud phase discrimination algorithm. *J. Atmos. Oceanic Technol.*, **26**, 2293–2309.
- Intrieri, J. M., M. D. Shupe, T. Uttal, and B. J. McCarthy, 2002: An annual cycle of Arctic cloud characteristics observed by radar and lidar at SHEBA. *J. Geophys. Res.*, **107** (C10), doi:10.1029/2000JC000423.
- Jäger, H., and T. Deshler, 2002: Lidar backscatter to extinction, mass and area conversions for stratospheric aerosols based on midlatitude balloonborne size distribution measurements. *Geophys. Res. Lett.*, **29**, 1929, doi:10.1029/2002GL015609.
- , and —, 2003: Correction to “Lidar backscatter to extinction, mass and area conversions for stratospheric aerosols based on midlatitude balloonborne size distribution measurements.” *Geophys. Res. Lett.*, **30**, 1382, doi:10.1029/2003GL0171892003.
- Kaul, B., I. Samokhvalov, and S. Volkov, 2004: Investigating particle orientation in cirrus clouds by measuring backscattering phase matrices with lidar. *Appl. Opt.*, **43**, 6620–6628.
- Kay, J., T. L'Ecuyer, A. Gettelman, G. Stephens, and C. O'Dell, 2008: The contribution of cloud and radiation anomalies to the 2007 Arctic sea ice extent minimum. *Geophys. Res. Lett.*, **35**, L08503, doi:10.1029/2008GL033451.
- Klett, J., 1981: Stable analytical inversion solution for processing lidar returns. *Appl. Opt.*, **20**, 211–220.
- Liu, Z., Z. Li, B. Liu, and R. Li, 2009: Analysis of saturation signal correction of the troposphere lidar. *Chin. Opt. Lett.*, **7**, 1051–1054.
- Lynch, D. K., S. D. Gedzelman, and A. B. Fraser, 1994: Subsuns, Bottlinger's rings, and elliptical halos. *Appl. Opt.*, **33**, 4580–4589.
- Magono, C., and C. W. Lee, 1966: Meteorological classification of natural snow crystals. *J. Fac. Sci., Hokkaido Univ.*, **2**, 321–335.
- Noel, V., and K. Sassen, 2005: Study of planar ice crystal orientations in ice clouds from scanning polarization lidar observations. *J. Appl. Meteor.*, **44**, 653–664.
- , and H. Chepfer, 2010: A global view of horizontally oriented crystals in ice clouds from Cloud-Aerosol Lidar and Infrared Pathfinder Satellite Observation (CALIPSO). *J. Geophys. Res.*, **115**, D00H23, doi:10.1029/2009JD012365.
- Nott, G. J., and T. Duck, 2011: Review: Lidar studies of the polar troposphere. *Meteor. Appl.*, **18**, 383–405.
- , and Coauthors, 2012: A remotely operated lidar for aerosol, temperature, and water vapor profiling in the High Arctic. *J. Atmos. Oceanic Technol.*, **29**, 221–234.
- Pal, S. R., and A. I. Carswell, 1973: Polarization properties of lidar backscattering from clouds. *Appl. Opt.*, **12**, 1530–1535.
- Pappalardo, G., and Coauthors, 2004: Aerosol lidar intercomparison in the framework of the EARLINET Project. 3. Raman lidar algorithm for aerosol extinction, backscatter, and lidar ratio. *Appl. Opt.*, **43**, 5370–5385.
- Platt, C., N. Abshire, and G. McNice, 1978: Some microphysical properties of an ice cloud from lidar observation of horizontally oriented crystals. *J. Appl. Meteor.*, **17**, 1220–1224.
- Rignot, E., and P. Kanagaratnam, 2006: Changes in the velocity structure of the Greenland Ice Sheet. *Science*, **311**, 986–990.
- Russell, P. B., T. J. Swissler, and M. P. McCormick, 1979: Methodology for error analysis and simulation of lidar aerosol measurements. *Appl. Opt.*, **18**, 1–15.
- Sassen, K., 1992: Evidence for liquid-phase cirrus cloud formation from volcanic aerosols: Climatic implications. *Science*, **257**, 516–519.
- , 2005: Polarization in lidar. *Lidar: Range-Resolved Optical Remote Sensing of the Atmosphere*, Springer, 19–40.
- , K.-N. Liou, Y. Takano, and V. I. Khvorostyanov, 2003: Diurnal effects in the composition of cirrus clouds. *Geophys. Res. Lett.*, **30**, 1539, doi:10.1029/2003GL017034.
- Schotland, R., K. Sassen, and R. Stone, 1971: Observations by lidar of linear depolarization ratios for hydrometeors. *J. Appl. Meteor.*, **10**, 1011–1017.

- Shupe, M. D., V. P. Walden, E. Eloranta, T. Uttal, J. R. Campbell, S. M. Starkweather, and M. Shiobara, 2011: Clouds at Arctic atmospheric observatories. Part I: Occurrence and macrophysical properties. *J. Appl. Meteor. Climatol.*, **50**, 626–644.
- , and Coauthors, 2013: High and dry: New observations of tropospheric and cloud properties above the Greenland Ice Sheet. *Bull. Amer. Meteor. Soc.*, **94**, 169–186.
- Starkweather, S. M., 2004: Characteristics of cloud cover and its radiative impacts over the high elevations of the Greenland Ice Sheet. Ph.D. thesis, University of Colorado, 202 pp.
- Stephens, G. L., 1978: Radiation profiles in extended water clouds. II: Parameterization schemes. *J. Atmos. Sci.*, **35**, 2123–2132.
- Takano, Y., 1989: Solar radiative transfer in cirrus clouds. Part I: Single-scattering and optical properties of hexagonal ice crystals. *J. Atmos. Sci.*, **46**, 3–19.
- Thayer, J., N. Nielsen, R. Warren, C. Heinselman, and J. Sohn, 1997: Rayleigh lidar system for middle atmosphere research in the Arctic. *Opt. Eng.*, **36**, 2045–2061.
- Thomas, L., J. Cartwright, and D. P. Wareing, 1990: Lidar observations of the horizontal orientation of ice crystals in cirrus clouds. *Tellus*, **42B**, 211–216.
- Turner, D., 2005: Arctic mixed-phase cloud properties from AERI lidar observations: Algorithm and results from SHEBA. *J. Appl. Meteor.*, **44**, 427–444.
- van de Hulst, H. C., 1981: *Light Scattering by Small Particles*. Dover, 487 pp.
- van den Broeke, M., and Coauthors, 2009: Partitioning recent Greenland mass loss. *Science*, **326**, 984–986.
- Washington, W., and G. Meehl, 1989: Climate sensitivity due to increased CO₂: Experiments with a coupled atmosphere and ocean general circulation model. *Climate Dyn.*, **4**, 1–38.
- Zhou, C., P. Yang, A. E. Dessler, Y. Hu, and B. A. Baum, 2012: Study of horizontally oriented ice crystals with CALIPSO observations and comparison with Monte Carlo radiative transfer simulations. *J. Appl. Meteor. Climatol.*, **51**, 1426–1439.